

Azimuthal Shear Wave Velocity Anisotropy in the Basin and Range Province Using Moho P_s Converted Phases

DANIEL E. MCNAMARA AND THOMAS J. OWENS

Department of Geological Sciences, University of South Carolina, Columbia

An eight-station large aperture seismometer array was deployed in the Basin and Range province of west-central Nevada for the 1988-1989 Program for Array Seismic Studies of the Continental Lithosphere (PASSCAL) Passive-source seismic experiment. During the 10 months of data collection a total of 100 teleseismic events were recorded ($\Delta > 30^\circ$). Source-equalized P wave receiver functions show waveform variations in timing, amplitude, and polarity in the Moho P_s phase that is diagnostic of shear wave velocity anisotropy. Information regarding the crustal anisotropic component can be recovered through the P_s phase since it is generated at the Moho and is sensitive to shear wave splitting in the crust only. We utilize single-event, stacked, and array-beam-formed receiver functions to minimize the influence of structural variations and scattering on the observed converted phases. Analysis of shear wave splitting of the P_s conversion from the crust-mantle boundary indicates a fast azimuth of anisotropy oriented approximately NW-SE with observed time delays of 0.20 s. This strongly suggests coherent crustal anisotropy with a fast direction perpendicular to the strike of fault block mountain ranges. This fabric is most likely due to the preferred crystallographic orientation of seismically anisotropic minerals in the middle to lower crust rather than the distribution of Basin and Range upper crustal fracture systems.

INTRODUCTION

Teleseismic waveform modeling, or receiver function analysis, is becoming a common method of examining crust and upper mantle structure. When applied to single three-component long-period seismic stations, the method has historically been used to delineate crustal thickness and occasionally other first-order details of the continental crust [Phinney, 1964; Burdick and Langston, 1977; Langston, 1977, 1979]. With the advent of broadband digital seismic stations in the early 1980s, higher-resolution crustal models could be determined beneath isolated stations [Owens *et al.*, 1984; Owens, 1987]. However, studies of single stations have always been limited by the natural distribution of passive teleseismic sources and hence have not been able to resolve more than first-order lateral variations in structure.

Recently, instrumentation developed by the Program for Array Seismic Studies of the Continental Lithosphere (PASSCAL) of the Incorporated Research Institutions for Seismology (IRIS) has created the potential for addressing this limitation through the deployment of arrays of seismic recorders. With this motivation, the 1988-1989 PASSCAL Basin and Range Passive Source Seismic Experiment deployed portable three-component seismic arrays in northwestern Nevada (Figure 1). The site of this experiment was chosen to coincide with the area studied by the 1986 PASSCAL Seismic Experiment [e.g., Benz *et al.*, 1990] and the 1983 Consortium for Continental Reflection Profiling (COCORP) 40° North profiles [Allmendinger *et al.*, 1987] which provide seismic refraction and reflection observations, respectively.

In addition to evaluating the applicability of seismic arrays in receiver function studies, which is being examined by Randall and Owens [1992], our scientific objectives focused on using P to S conversions in the coda of the teleseismic P wave to better

define the structure and tectonic processes active in the Basin and Range. Within this context, this paper examines shear wave splitting observed in P to S converted phases (P_s phases) generated at the crust-mantle boundary. These observations, the first of their kind to our knowledge, are unique in that the source of the shear wave splitting must lie above the Moho. Thus they provide an excellent means of studying the nature of vertically averaged shear wave anisotropy in the crust.

GEOPHYSICAL OVERVIEW OF THE BASIN AND RANGE

The Basin and Range has had a tectonically active history that has been the focus of many geological and geophysical studies [e.g., Pakiser, 1963; Eaton, 1963; Prodehl, 1979; Zoback, 1989; Taylor and Paton, 1986; Lachenbruch and Sass, 1978; Farmer and DePaolo, 1983]. The current physiography of the Basin and Range is a result of crustal extension beginning in the late Oligocene [Speed *et al.*, 1987]. The Basin and Range is characterized by fault block mountains and sediment-filled basins and is currently a region of active continental extension between two relatively stable crustal blocks: the Colorado Plateau to the east and the Sierra Nevada to the west. A NNW directed spreading rate of approximately 10 mm/yr has resulted in nearly 250 km of Cenozoic extension in the northern Basin and Range [Thompson and Burke, 1974; Minster and Jordan, 1987; DeMets *et al.*, 1987].

Interpretations of data from previous seismic experiments in the Basin and Range show the crust to range in thickness from 20 to 40 km [Prodehl, 1970; 1979; Eaton, 1963; Stauber and Boore, 1978; Priestley *et al.*, 1982; Klempner *et al.*, 1986; Allmendinger *et al.*, 1987; Hague *et al.*, 1987; Stauber, 1983]. To further resolve the geophysical characteristics of the Basin and Range, a combination reflection and refraction seismic experiment was conducted in 1986 (Figure 1). One- and two-dimensional raytrace modeling of the refraction data indicates that lateral variations in crustal thicknesses in northwestern Nevada range between 29 and 37 km [Benz *et al.*, 1990]. This agrees quite well with the results from 1986 PASSCAL reflection

Copyright 1993 by the American Geophysical Union.

Paper number 93JB00711.
0148-0227/93/93JB-00711\$05.00

spreads [Holbrook, 1990; Holbrook *et al.*, 1991; Catchings and Mooney, 1991] and the two-way travel times of near vertical Moho reflections collected in 1983 by COCORP [Klemperer *et al.*, 1986]. COCORP recorded deep reflection profiles across northern Nevada and found a prominent band of reflections with two-way travel times of 9.5 to 10.5 s [Klemperer *et al.*, 1986] that marks the transition between an overlying reflective fabric and an underlying nonreflective zone. The calculated depth to this band is 29 to 30 km and is assumed to be the top of the reflection Moho [Klemperer *et al.*, 1986]. The Basin and Range crust/mantle transition has been modeled by the 1986 PASSCAL Nevada active source experiment as a 2-km-thick gradient zone (7.3-7.6 km/s) with an underlying mantle increasing in velocity from 7.8 km/s to 8.2 km/s with depth [Holbrook, 1990; Catchings and Mooney, 1991]. The variation in all results, when taken together, suggest a youthful lower crust/upper mantle and a prominent Moho with a thickness of 2 to 3 km.

Observations of azimuthal velocity variations are not uncommon for the Basin and Range. Experiments using Pn travel times and amplitudes to analyze anisotropy in the mantle lid, directly beneath the Basin and Range, had results similar to those that we present here [Beghoul and Baranzangi, 1990; Holbrook, 1990]. Their observed direction of maximum seismic velocity coincides with the NW-SE direction of present-day tectonic extension. Azimuthal velocity variations were also observed in regionalized surface-wave dispersion analysis [Taylor and Patton, 1986]. Savage *et al.* [1990b] attributed shear wave splitting of direct S and SKS phases, recorded in western Nevada, to a 100-km-thick anisotropic mantle layer. They associated a WNW shear polarization direction with pre-Miocene Basin and Range crustal extension.

THE 1988-1989 PASSCAL PASSIVE SOURCE EXPERIMENT

The field portion of the experiment consisted of two passive source seismometer arrays with differing passbands and apertures (Figure 1). A large aperture array (LAA) of eight intermediate period three-component stations was deployed for 10 months for the collection of teleseismic waveforms. The average station spacing for the LAA was approximately 10 km. At each LAA site were a PASSCAL data logger and Kinematics SV-1/SH-1 (5-s natural period) sensors operating independently in event-triggered mode. This experiment was the first long-term deployment of this prototype PASSCAL instrumentation. The array was located approximately 65 km east of Lovelock, Nevada, in Buena Vista Valley between the Humboldt Range to the west and the Stillwater Range to the east. It was centered at the intersection of the two refraction/reflection lines of the 1986 PASSCAL Nevada Experiment (Figure 1). Most site locations were at or near bedrock (Table 1). In addition, a small aperture array (SAA) with 12 three-component short-period (1 Hz) seismometers was deployed around station FNC (Figure 1). Average station spacing for the inner SAA was approximately 2.5 km. The SAA was equipped with 1-s Geotech S-13 sensors and operated continuously for three months with digital telemetry to a central recording site. The equipment for the SAA was part of the "Configurable Seismic Monitoring Network" developed at Lawrence Livermore National Laboratory [Nakanishi *et al.*, 1991].

This study is restricted to the LAA data because the array's long deployment period and instrument passband of the array was most appropriate for the analysis of teleseismic P waves. The 1988-1989 PASSCAL seismic experiment recorded 214 seismic

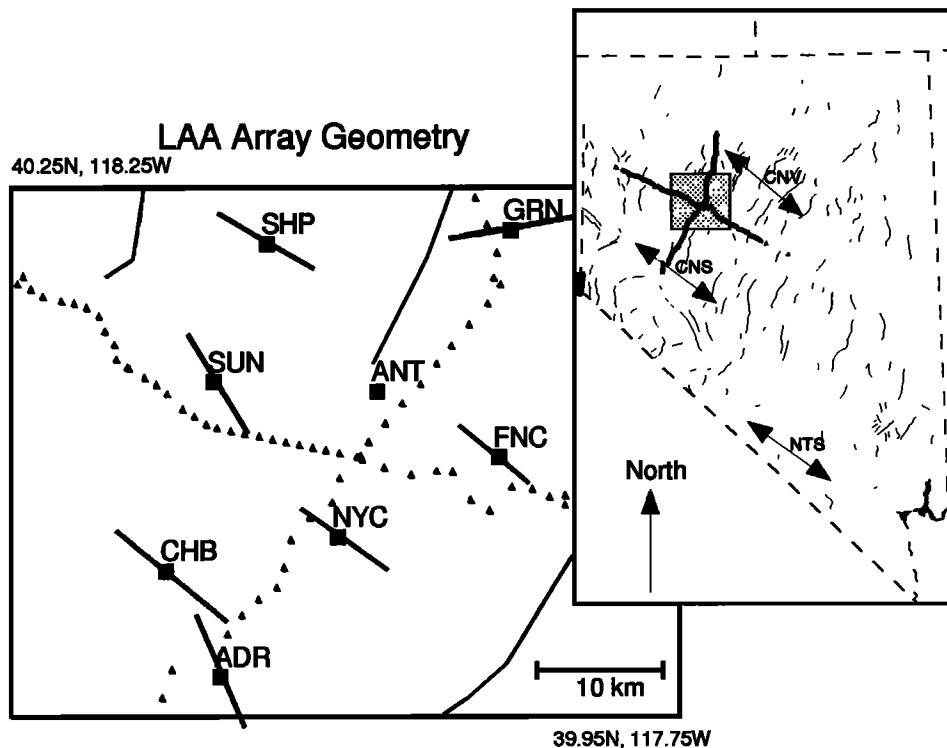


Fig. 1. Base map of 1988-1989 the Program for Array Seismic Studies of the Continental Lithosphere (PASSCAL) field deployment. The array is located in Nevada at the intersection of refraction/reflection lines shot during the 1986 PASSCAL active source experiment. Large aperture array (LAA) station locations are shown as boxes; triangles are 1986 instrument sites. The relationship between regional stress field and computed fast azimuth is shown. Fast azimuth and splitting averages are shown as a vector at each LAA station. See Table 4 for estimates at each individual station. Three measurement locations of the direction of maximum tensile stress are shown at CNV [Zoback, 1989], CNS [Doser, 1986] and CNT [Stock and Healy, 1988].

TABLE 1. Large Aperture Array Station Locations

Station	Latitude,°N	Longitude,°E	Elevation,m	Station Name
ADR	39.972	118.094	1520.0	Anderson Ranch
ANT*	40.113	117.974	1241.7	Antelope
CHB	40.032	118.133	1347.0	Chocolate Butte
FNC*	40.096	117.885	1487.0	Fencemaker Flat
GRN	40.218	117.878	1317.0	Granite Hills
NYC	40.051	118.007	1475.0	New York Canyon
SHP	40.217	118.058	1341.0	Shiprock
SUN	40.139	118.099	1335.0	Sunnyside

*site not on bedrock

events with known locations during the 10-month LAA deployment. 100 teleseismic events ($\Delta > 30^\circ$) were recorded with body wave magnitudes ranging from 4.7 to 6.7. Back azimuthal coverage is normal for North America with the best coverage from the southwest due to the seismically active regions of the South Pacific (Table 2). Each LAA site triggered on the basis of the ratio between a 100s long-term average and a 6s short-term average. When triggered, 30 s pre-trigger and 120 s post-trigger of data were recorded at 20 samples/s. We performed routine calibration on all components during service visits. These calibration pulses were inverted to obtain best fit free period, damping, and amplitude relative to the vertical sensor. Sensor parameters did not vary significantly during the course of the deployment. A complete data report with comprehensive information on event locations and seismometer calibration data is available from the IRIS Data Management Center and has been described by *Owens and Randal* [1990].

QUALITATIVE RECEIVER FUNCTION ANALYSIS

To utilize teleseismic *P* waveforms, we must isolate the response of the crust and upper mantle structure beneath the station, the receiver function, from the source and mantle path

effects which also have an influence on the recorded seismogram using source deconvolution (for a review, see *Langston* [1979]; *Ammon* [1991]; and *Owens et al.*, [1984]. In this processing, we cut each event to a length of 120 seconds (30 s pre-event, 90 s post-event), remove the mean, and apply a Hanning taper to the leading and trailing 5 s of the traces. Horizontal seismograms are rotated to the theoretical radial and tangential components, and the vertical component is deconvolved from them in the frequency domain with water level stabilization [*Langston*, 1979]. A simple Gaussian time pulse is convolved with the resulting horizontal receiver functions. In this study, the Gaussian serves as a 1-Hz low-pass filter to smooth the receiver functions. The resulting horizontal receiver functions are primarily sensitive to the shear velocity structure beneath the receiver [*Owens et al.*, 1984].

Preliminary analysis of teleseismic *P* waveform receiver functions generated from the LAA data reveals several relevant observations. A strong secondary phase, on the radial component, approximately 3.5 s behind the direct *P* arrival, has been observed and interpreted to be the *Ps* conversion from the crust-mantle boundary. The phase consistently arrives from all back azimuths and is the only arrival in the *P* wave coda with significant amplitude when several events are stacked from similar back azimuths (Figure 2). Using a model supplied from the

TABLE 2. Event Locations

Event	Date	Origin Time,UT	Latitude,°N	Longitude,°E	Depth,km	Mb
001	Aug. 17, 1988	0159:11.1	7.658S	107.264E	58	6.0
002	Aug. 17, 1988	1134:52.4	26.912S	70.855W	39	5.6
003	Aug. 17, 1988	1238:13.7	27.208S	70.812W	37	5.3
004	Aug. 20, 1988	2309:10.3	26.663N	86.620E	70	6.5
006	Aug. 21, 1988	1351:43.4	42.795S	85.877W	10	5.8
009	Aug. 27, 1988	0125:17.7	11.303N	141.455E	33	5.2
010	Aug. 27, 1988	1630:17.6	15.838S	172.144W	33	6.0
015	Sept. 01, 1988	1652:52.3	17.065N	99.265W	33	5.0
016	Sept. 02, 1988	1027:48.5	54.030N	161.491E	47	5.1
017	Sept. 05, 1988	0613:18.7	18.532N	70.391W	33	5.5
018	Sept. 07, 1988	1153:25.4	30.336N	137.364E	499	6.0
019	Sept. 13, 1988	0058:45.9	29.806N	138.364E	447	5.8
020	Sept. 14, 1988	0359:57.4	49.801N	78.791E	0	6.1
021	Sept. 14, 1988	2214:07.6	23.387S	67.945W	124	5.8
022	Sept. 15, 1988	1848:03.2	1.404S	77.896W	189	5.8
023	Sept. 16, 1988	0006:52.9	22.952S	175.413W	33	4.9
024	Sept. 16, 1988	0216:14.9	20.362S	178.364W	500	5.2
025	Sept. 16, 1988	0245:35.8	20.170S	177.770W	500	4.7
026	Sept. 16, 1988	0627:29.0	17.785S	169.065E	33	4.9
028	Sept. 17, 1988	1523:53.7	44.910N	152.945E	43	5.3
032	Sept. 19, 1988	1858:37.7	23.003S	175.508W	33	5.4
035	Sept. 21, 1988	0958:51.8	46.129N	152.142E	38	5.9
038	Sept. 21, 1988	2359:26.7	16.073S	173.481W	33	5.5
040	Sept. 22, 1988	2228:36.3	23.030N	167.860W	10	5.5
042	Sept. 26, 1988	0823:21.4	35.402N	140.864E	45	5.9
047	Sept. 30, 1988	2145:01.1	19.356S	177.555W	548	5.4
048	Oct. 01, 1988	0943:24.5	35.305S	106.059W	10	5.6
050	Oct. 03, 1988	0045:57.8	10.227S	161.243E	130	5.5

TABLE 2. (continued)

Event	Date	Origin Time,UT	Latitude,°N	Longitude,°E	Depth,km	Mb
052	Oct. 04, 1988	1537:57.7	3.533S	150.437E	33	5.4
053	Oct. 08, 1988	0446:24.4	18.693S	172.429W	33	6.7
057	Oct. 10, 1988	0552:11.6	42.830N	144.230E	63	5.6
058	Oct. 10, 1988	0719:21.2	23.161S	171.969E	33	5.6
059	Oct. 10, 1988	1820:30.0	28.344S	177.670W	57	6.5
060	Oct. 11, 1988	1330:05.1	40.279N	125.632W	10	3.6
063	Oct. 17, 1988	0556:53.5	51.237N	159.551E	33	5.7
068	Oct. 19, 1988	0008:41.2	36.987N	141.701E	49	5.6
075	Oct. 22, 1988	1604:13.4	49.061N	156.179E	50	5.6
076	Oct. 23, 1988	0637:45.0	49.120N	156.215E	33	5.6
077	Oct. 23, 1988	1338:11.1	49.205N	156.239E	33	5.3
086	Oct. 28, 1988	1449:30.2	16.198S	174.342W	140	5.4
088	Oct. 31, 1988	0208:12.5	23.305S	66.665W	204	5.0
090	Nov. 03, 1988	144:711.1	13.793N	90.696W	69	5.6
092	Nov. 07, 1988	0350:02.8	22.179S	175.008E	33	5.6
101	Nov. 25, 1988	2346:02.9	48.124N	71.246W	20	5.9
104	Dec. 05, 1988	1605:31.4	15.320S	173.400W	33	6.1
105	Dec. 07, 1988	0741:24.2	40.949N	44.293E	10	6.2
106	Dec. 07, 1988	0745:44.2	41.056N	44.481E	10	5.8
109	Dec. 08, 1988	1258:59.8	6.876N	82.827W	10	5.7
112	Dec. 13, 1988	0401:38.9	71.067N	7.775W	10	5.7
115	Dec. 16, 1988	0957:17.4	29.670S	178.000W	33	6.2
118	Dec. 24, 1988	0426:57.5	23.386S	66.392W	223	5.9
119	Jan. 02, 1989	0152:10.4	18.326S	174.548W	122	6.0
120	Jan. 03, 1989	0441:11.2	29.526N	131.454E	33	5.7
122	Jan. 09, 1989	1342:37.2	46.794N	153.733E	33	5.9
125	Jan. 12, 1989	1947:40.5	46.694N	153.981E	33	5.6
126	Jan. 13, 1989	1801:56.2	46.497N	153.662E	33	5.6
130	Jan. 22, 1989	2220:18.8	41.742N	144.359E	33	6.0
132	Jan. 27, 1989	0834:51.9	56.188N	164.440E	33	5.8
134	Jan. 31, 1989	1739:25.3	22.292N	107.179W	10	5.2
135	Feb. 04, 1989	1924:11.2	5.929N	82.808W	33	5.8
136	Feb. 07, 1989	0403:00.5	21.852S	66.931W	179	5.4
137	Feb. 10, 1989	1115:26.7	3.03N	126.92E	33	6.0
139	Feb. 13, 1989	1451:24.4	57.460N	33.107W	10	5.2
140	Feb. 13, 1989	1514:47.4	57.409N	33.279W	10	5.2
141	Feb. 14, 1989	0620:26.9	10.434S	161.283E	78	6.1
144	Feb. 16, 1989	2150:37.8	45.327N	151.785E	95	5.7
146	Feb. 22, 1989	1025:41.4	56.217N	153.629W	7	5.7
148	Feb. 25, 1989	1126:37.7	29.759S	177.918W	47	6.4
150	Feb. 28, 1989	1301:57.9	23.086S	61.585W	575	5.5
151	March 01, 1989	0242:02.2	43.769N	148.985E	44	5.7
152	March 02, 1989	0713:45.6	18.413N	68.676W	129	5.4
153	March 06, 1989	1439:42.0	35.800N	140.400E	33	5.7
156	March 11, 1989	0504:54.3	17.723S	174.798W	175	6.3
159	March 16, 1989	0934:00.5	29.992S	178.119W	57	5.7
160	March 17, 1989	1933:06.9	34.350S	178.650W	44	5.9
161	March 20, 1989	0106:33.1	59.927N	153.718W	127	5.0
214	March 30, 1989	2039:29.6	19.371S	176.052W	229	5.5
167	April 05, 1989	2347:48.3	21.135S	69.211W	114	5.8
168	April 06, 1989	0805:40.0	19.602S	169.467E	33	6.3
169	April 07, 1989	1332:11.6	51.337N	30.008W	10	5.1
171	April 08, 1989	0122:20.5	57.251N	143.615W	10	4.9
172	April 08, 1989	0306:01.4	15.680S	173.004W	33	5.5
173	April 09, 1989	0507:50.3	51.533N	178.440W	32	5.2
174	April 11, 1989	0356:38.8	49.387N	159.259E	33	6.3
175	April 13, 1989	0043:11.2	39.488S	75.081W	33	5.9
176	April 14, 1989	1252:09.2	19.200N	144.860E	33	5.8
177	April 14, 1989	1302:47.8	18.052S	178.423W	571	5.4
178	April 15, 1989	1426:41.6	8.430N	61.070W	25	5.8
179	April 15, 1989	2034:11.5	30.021N	99.321E	33	6.2
180	April 16, 1989	1051:16.6	4.735N	32.671W	10	5.4
181	April 16, 1989	1948:14.9	20.989S	179.034W	611	5.6
182	April 18, 1989	1233:53.6	23.718S	179.914E	536	5.8
196	April 19, 1989	0008:22.9	31.323S	177.906W	33	5.8
183	April 19, 1989	1448:56.0	17.859N	105.303W	10	5.1
185	April 20, 1989	0808:51.5	9.170S	79.034W	64	5.7
187	April 20, 1989	2259:54.9	57.123N	121.950E	33	6.0
190	April 23, 1989	1921:10.0	66.918N	156.241W	33	5.7
191	April 25, 1989	0213:24.5	30.042N	99.477E	33	6.1
192	April 25, 1989	1429:01.1	16.874N	99.411W	23	6.4
193	April 25, 1989	1718:37.9	35.890N	140.414E	71	5.4
194	April 27, 1989	0220:05.8	30.694N	140.734E	93	6.0
212	April 28, 1989	0748:16.0	13.100N	89.700W	33	5.8
213	April 28, 1989	0234:25.0	17.800N	105.200W	33	5.8

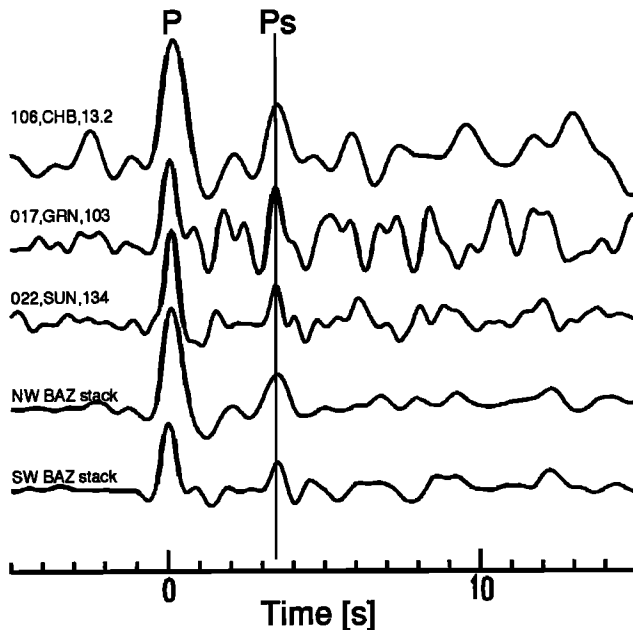


Fig. 2. Single estimated radial receiver functions and stacks of multiple receiver functions from several back azimuths. Notice the consistency of the Moho P_s phase approximately 3.5 seconds after the direct P arrival. Seismograms are labeled with event number, station and back azimuth. There are 29 events in the NW back azimuth stack and 21 in the SW back azimuth stack.

1986 PASSCAL Nevada experiment [Benz *et al.*, 1990], we calculated synthetic radial receiver functions for comparison with our observations. Timing and amplitude for the Moho P_s phase from observed and synthetic receiver functions indicate a crustal thickness of approximately 28 km [Owens *et al.*, 1989]. The Moho P_s phase converts from a P wave to an S wave nearly directly beneath the receiving station. For a 28-km-thick crust of average S velocity, 3.6 km/s, the Moho P_s is generated only 5 km laterally from the site and arrives at an angle less than 10° off vertical from a teleseism at a distance of 80° . Thus it provides a very site-specific sample of the crust beneath each station.

For the purpose of this study, the most important observation is that the crustal response observed in the receiver functions is simple in that there is no evidence for strong arrivals from the middle and lower crust. Thus the P_s phase from the Moho can be unambiguously picked for further study. We have observed deviations from a simple crustal model as slight variations in the P_s phase arrival times (0.2 s) across the array. Radial component arrival time variations indicate a crustal thickening of 1–1.5 km across the LAA consistent with a southeast dipping Moho. two-dimensional models from the 1986 PASSCAL Nevada experiment show an eastward thickening crust with, however, a relatively flat Moho beneath our array [Holbrook, 1990; Catchings and Mooney, 1991]. Interpretations by Benz *et al.*, [1990] from the same experiment may also indicate eastward thickening. They found that Moho depths are greater in one-dimensional models at the eastern end of the profile (Figure 1).

In addition to variations in timing of the Moho P_s observed on the radial component, our initial analysis also reveals arrivals on the tangential component of motion (Figure 3). This indicates a departure from an Earth consisting of flat homogeneous isotropic layers since such an Earth would produce no tangential energy. In our data we find examples where the tangential component arrival is energetic and clearly associated with the radial P_s

arrival, but the tangential component arrives slightly early relative to the radial arrival (Figure 3c). It appears that the components are made up of two arrivals with slightly different propagation velocities. In other cases, evidence for a "split" P_s phase exists but is less definitive (Figures 3a and 3b). Finally, at some back azimuths there appears to be little tangential energy associated with the radial P_s (Figure 3d). With the isolated observations of the type shown in Figure 3 it would be difficult to develop a coherent model of the cause of this phenomenon. However, the LAA allow us to observe nearly 100 receiver functions at seven sites. The consistency and repeatability of these observations allows us to make a strong argument that the observed behavior is in fact shear wave splitting due to azimuthal anisotropy in the Basin and Range crust.

In previous receiver function studies, tangential energy has been explained by either planar dipping interfaces [Langston, 1977; Owens and Crosson, 1988] or scattering [Langston, 1989; Randall and Owens, 1992]. Layer dip leaves a characteristic signature on tangential receiver functions in that their amplitude should be zero for events arriving along the dip direction and should grow to a maximum for events arriving along strike. For small dip values, the effect on the radial component is small. Since some southeastward crustal thickening is indicated in the area [Holbrook, 1990; Holbrook *et al.*, 1991], we would expect dip to be contributing to the observed tangential energy. However, the fundamental difference between our observations and a dipping layer response is the existence of "split" P_s phases in our data. Dipping layers cannot produce this effect, and thus we must consider other phenomena.

The influence of scattering due to small-scale heterogeneities on receiver functions has only recently begun to be quantified [Langston, 1989; Randall and Owens, 1992]. Scattering can result in low to moderate amplitude energy on both the radial and tangential components of receiver functions that is not necessarily correlated from event to event. This can induce elliptical particle motion that is not related to any inherent physical property, such as anisotropy. Thus scattering could produce "false" splitting observations in certain circumstances, or it could contaminate the true splitting observations. We address this problem in our analysis in two ways. First, we use over 100 single-station receiver functions and several stacked receiver functions. Second, we take advantage of our ability to use beamforming to enhance the coherent part of the receiver response.

P_s PHASE SHEAR WAVE SPLITTING

Any material whose properties vary with direction is anisotropic, and seismic waves penetrating such material will behave much differently than they would if propagating through an isotropic media. Figure 4 schematically shows the effects of shear wave splitting on Moho P_s phases. Initially, a near-vertically incident P wave generates a radially polarized converted shear wave at the crust-mantle boundary. The shear wave upon entering the anisotropic region splits into two phases with polarizations and velocities that mimic the properties of the anisotropic media. The phases, polarized into fast and slow directions, progressively split in time as they propagate through the anisotropic media. This split is preserved in any isotropic segments along the ray path and can be observed as a time delay (dt) between the two horizontal components of motion (Figure 4). Polarity and amplitude are strongly affected by the azimuth of arrival. Anisotropy also leaves a characteristic signature on the tangential com-

ponent of receiver functions. In contrast to the case of a dipping layer, the tangential component will be zero along both the fast and slow azimuth directions and reach a maximum 45° from either axis [Silver and Chan, 1988; Bowman and Ando, 1987; Savage et al., 1990a; Kosarev et al., 1984].

Figure 3 shows examples of P_s wave timing, amplitude, and polarity variations from all four geographic quadrants. The seismograms are deconvolved as described earlier and show that in some places there is a clear time split between the radial and tangential components of motion (Figures 3a and 3b). This observation can also be seen in horizontal component particle motion polarization diagrams (Figure 5). The existence of elliptical particle motion, as seen in Figure 5a, rather than rectilinear particle motion has often been used to interpret the deviation from an isotropic Earth in terms of seismic velocity anisotropy [e.g. example, Silver and Chan, 1988; Bowman and Ando, 1987; Savage et al., 1990a; Shih et al., 1989]. We also observed several receiver functions with nearly zero tangential amplitude for Moho P_s phases and linear horizontal particle motion from both the northwest and southeast back azimuth quadrants. In the presence of anisotropy this could be interpreted as an arrival along either the fast or slow azimuth (Figure 5b) [Silver and Chan, 1991; Kosarev et al., 1984].

Our comparison of stacked receiver functions from the southwest (average back azimuth = 234°) and stacks from the

west-southwest (average back azimuth = 262°) showed that the largest amplitudes of tangential energy in the data were observed for events arriving from a more western back azimuth (Figure 3c). This would suggest that the axes of anisotropy should be oriented roughly northwest-southeast and northeast-southwest. In contrast, a stack of events arriving from the northwest (average back azimuth = 307°) showed that while the radial P_s component is well defined, there is little tangential energy observed in the waveforms. We searched the data for receiver functions with P_s phase tangential amplitudes that fell below the noise level of the individual seismograms prior to the direct P arrival and found 48 station-event pairs, all arriving either from the northwest or the southeast (Figure 6). This strongly suggests that some form of crustal inhomogeneity with a northwest-southeast preferred orientation is producing the observed P_s phase variations.

ESTIMATION OF DEGREE AND ORIENTATION OF ANISOTROPY

Beyond the preliminary analysis of P_s phase amplitude and polarity, we have used three methods to analyze splitting in the P_s phase. All methods are similar in that they attempt to estimate the orientation and degree of anisotropy. Orientation is estimated by determining the direction of the fast azimuth of anisotropy (ϕ), and the degree of anisotropy is estimated by

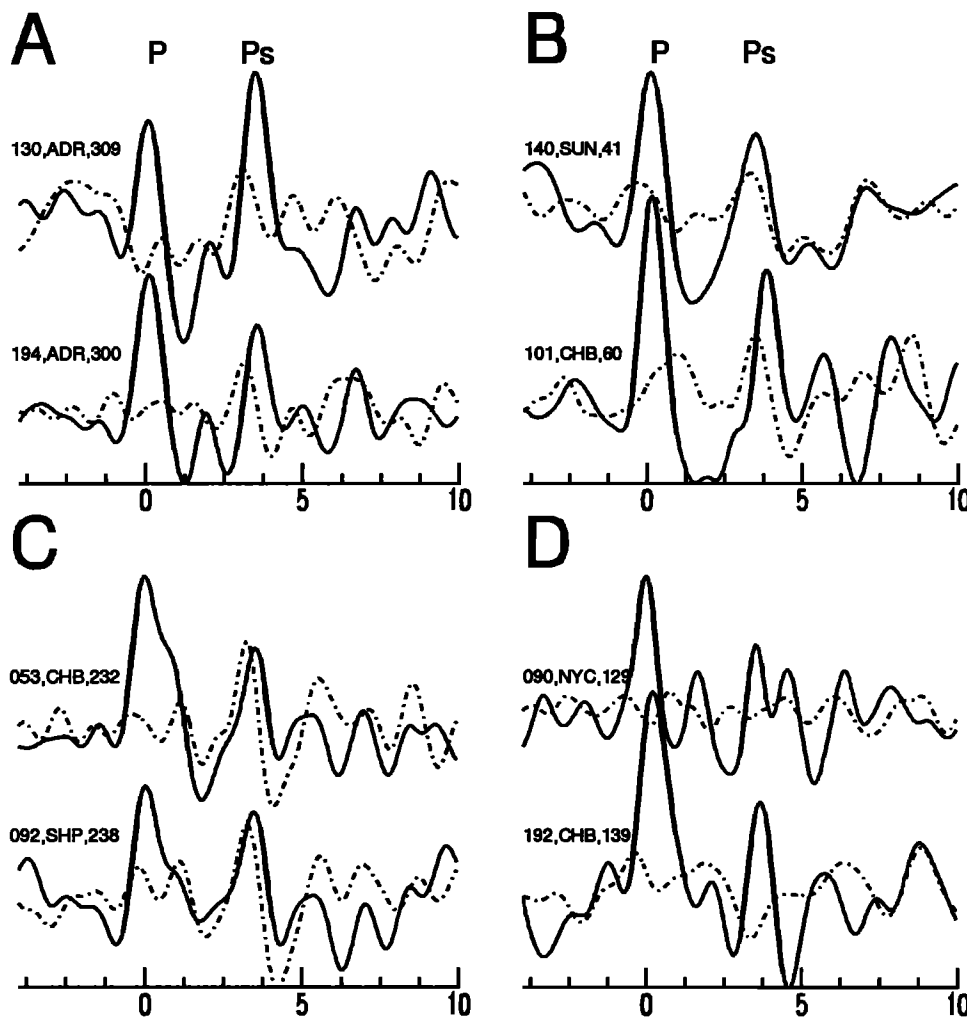


Fig. 3. Observed shear wave splitting in the P_s phase from several back azimuths. Solid line is the radial component and dashed line is the tangential component. Seismograms are labeled with event number, station and back azimuth.

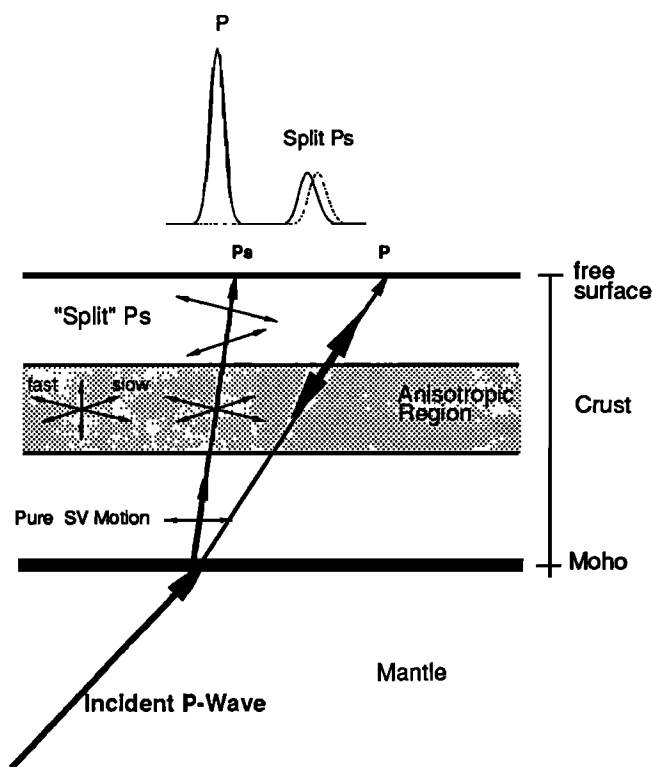


Fig. 4. The effects of shear wave splitting in the Moho P to S converted phase. Top shows a schematic seismogram in the fast/slow coordinate system with split horizontal P_s components.

measuring the time split (dt) between the fast and slow components of motion. We selected only seismograms with impulsive P_s phases and relatively high signal-to-noise ratios for analysis. Since particle motion is a good diagnostic of shear wave splitting, we examined initial horizontal motion of the P_s phase. Those with initial linear motion and an impulsive radial P_s were assumed to be arriving along an axis of anisotropy and are plotted in Figure 6 [Silver and Chan, 1988, 1991; Kosarev et al., 1984]. P_s phases with initial elliptical particle motion in the radial-tangential coordinate system were selected and processed using the three procedures described in this section.

Particle motion analysis. Polarization anomalies induced by the effects of anisotropy are best seen in particle motion diagrams as departures from rectilinear particle motion. Shear wave splitting produces significantly more elliptical particle motion (relative to an isotropic Earth) that is initially polarized in the ϕ -direction (fast azimuth direction). Shear wave splitting and resultant particle motion anomalies are the principle diagnostic properties used to estimate ϕ and dt in a number of techniques [Bowman and Ando, 1987; Silver and Chan, 1988; Savage et al., 1990a; Savage et al., 1989; Silver and Chan, 1991; Shih et al., 1989].

In our first method, the orientation of initial particle motion is measured from a horizontal particle motion plot of the radial and tangential components of the receiver functions and is taken to be a measure of ϕ . The receiver functions are then rotated to a coordinate system defined by the P_s phase initial particle motion. In this coordinate system, dt can be directly measured as the time delay between the fast and slow P_s phases using a cross-correlation procedure. For the cross-correlation computation, a P_s phase window for each seismogram was determined to include the beginning of the P_s phase on the fast component and the end of the P_s phase on the slow component. The cross-correlation

coefficient was computed for time lags of -2 to $+2$ s to ensure a complete pass of the two waveforms. The time lag producing the maximum or minimum coefficient is considered a measure of the splitting, dt , between the two shear waves. The seismograms are then shifted by the appropriate time lag rotated back to the original radial/tangential coordinate system, and the "corrected" P_s phase particle motion is plotted. If estimates of ϕ and dt have successfully removed the effects of anisotropy, the resulting particle motion will be significantly more linear than the original.

Waveform cross correlation. In this procedure, we seek to take advantage of the fact that in the fast-slow coordinate system, the components of the split P_s phase will be most similar. This is similar to the methods used by Bowman and Ando [1987]. The receiver functions were rotated in 5° increments from 0° to 180° , and at each increment the maximum and minimum cross-correlation coefficient is computed from time lags of -0.5 to $+0.5$ s. The angle of rotation resulting in the maximum absolute value of the cross-correlation coefficient is taken as a measure of ϕ . The procedure used to estimate dt once ϕ is determined is the same as in our particle motion analysis.

Tangential energy minimization. This method is an implementation of the technique of Silver and Chan [1988]. Any P to S converted phase will normally be radially polarized; therefore the existence of tangential energy argues for the presence of nonhomogeneous structure. Silver and Chan [1988] assumed that this tangential energy is entirely due to anisotropy and devised a grid search method to determine the ϕ - dt pair that most effectively minimizes the energy on the tangential component of motion of receiver functions rotated to the coordinate system defined by ϕ and shifted by dt . In our implementation, we applied the minimization measure of Silver and Chan [1988] within the P_s phase window for each ϕ - dt pair in a grid with 1° increments in ϕ and 0.05 increments in dt . We found that this method produced results that were not realistic. Estimates of dt routinely were between 0.4 and 0.5 s, which are unrealistic for the crust; the determinations of ϕ spanned all azimuths.

We believe that this method failed for two reasons. First, since the signal-to-noise ratio in the P_s coda is rarely more than 3, rigorous minimization of the tangential component is not as stable as it was for the high signal-to-noise ratio SKS phases for which the method was developed. In another study Silver and Chan [1991] found that the tangential energy minimization method of Silver and Chan [1988] should be used only with a relatively noise free seismogram. Second, the energy on the tangential component is not due simply to anisotropy; rather, it is due to a combination of anisotropy, dipping layers, scattering, and noise. Thus information regarding ϕ and dt were not obtainable using this method. The consistency of the first two methods we used and the fact that the ϕ - dt pairs obtained always reduced the tangential component as seen in our visual inspections indicates that we have found appropriate ϕ - dt pairs using these methods. Thus we did not pursue the tangential energy minimization procedure further.

Anisotropy estimate results. A total of 74 receiver functions from 46 different events were analyzed using the particle motion and waveform cross-correlation methods. In addition, 48 receiver functions from 29 events which had P_s phases with near-zero tangential component or a split time of less than 0.10 s were considered to have linear particle motion and were plotted in Figure 6.

Final ϕ and dt estimates were given qualitative quality rankings based on a number of factors. These included signal-to-noise ratio, magnitude of dt estimate, and linearization of particle

motion by ϕ - dt pair. Estimates were considered successful when corrected particle motion was linearized, waveforms were similar in shape in the fast/slow coordinate system, P_s phase tangential energy was reduced in the corrected seismogram, and dt estimate was 0.35 s or less. We judged 0.35 s as the upper limit of geologically realistic split times in a 30 -km-thick crust. Of the 74 receiver functions analyzed for this study, 20 were discarded due to low quality estimates based on the above criteria. The remaining 54 were qualitatively ranked in quality as A or B, with A indicating estimates we judged as excellent. Final estimates of ϕ and dt were determined by averaging the results of the two procedures we used, except in the cases where the results disagreed substantially. In these cases, the differences could usually be attributed to difficulties in estimating the direction of initial P_s polarization in the first procedure due to pre- P_s noise levels, and thus the waveform cross-correlation result was used. These events are marked with an asterisk in the quality column of Table 3.

The vector mean fast azimuth direction for the entire data set is 127° , while the mean for the 29 A ranked events is 145° . When higher-quality events are used, scatter in the estimate is decreased and the value of ϕ rotates southward. The final dt estimates are slightly less scattered than the estimates of ϕ . The

average dt was 0.24 s for the A ranked estimates. The A quality estimates are plotted in Figure 7.

As a final consistency check of our ϕ - dt estimates, we chose 20 high-quality receiver functions and stacked them in the average fast-slow coordinate system. We selected a ϕ of 135° because it is the approximate median of the ϕ estimates for A quality events and the entire data set. We selected the events so as to cover all geographic quadrants. Each component in the stack was multiplied by either +1 or -1, depending on the polarities predicted by P_s phase synthetics [McNamara, 1990] so that each trace should have a positive polarity P_s phase on both the fast and slow components of motion. The resulting traces show excellent similarity in shape between the two components and a well-defined splitting with $dt = 0.24$ s (Figure 8). This suggests that the ϕ - dt pairs derived from the above analysis are appropriate estimates of splitting of the P_s phase from the Moho due to azimuthal velocity anisotropy in the Basin and Range crust.

Estimates of anisotropy parameters for individual stations for all A and B ranked events are tabulated in Table 4. With the exception of site GRN, all the estimates are consistent with the values obtained for the entire data set. GRN is anomalous in several ways. First, it has only two A quality estimates of anisotropic properties; Second, it is located along a northeast-

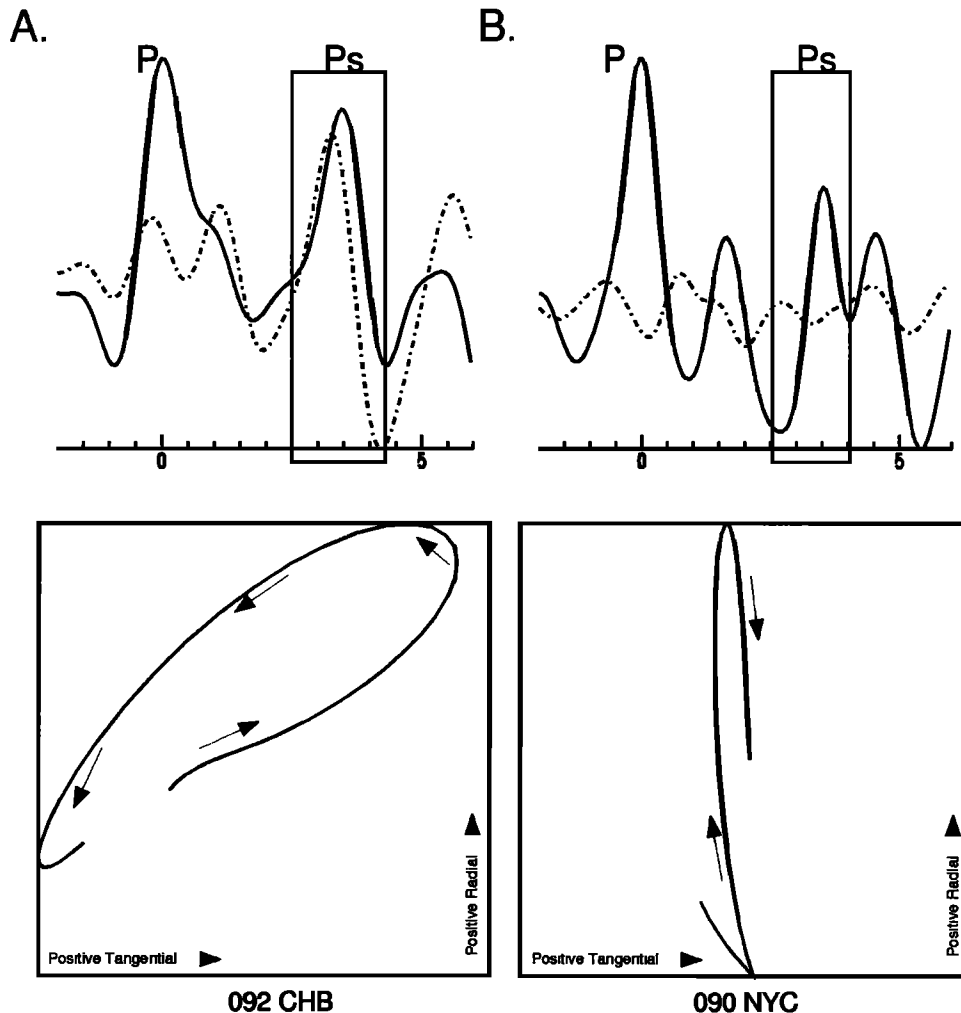


Fig. 5. Horizontal component P_s phase polarization diagrams. (a) Elliptical motion (event 092 at CHB, BAZ = 238°) suggests the existence of shear wave velocity anisotropy. (b) Initial linear particle motion directed NW to SE (event 090 at NYC, BAZ = 130°).

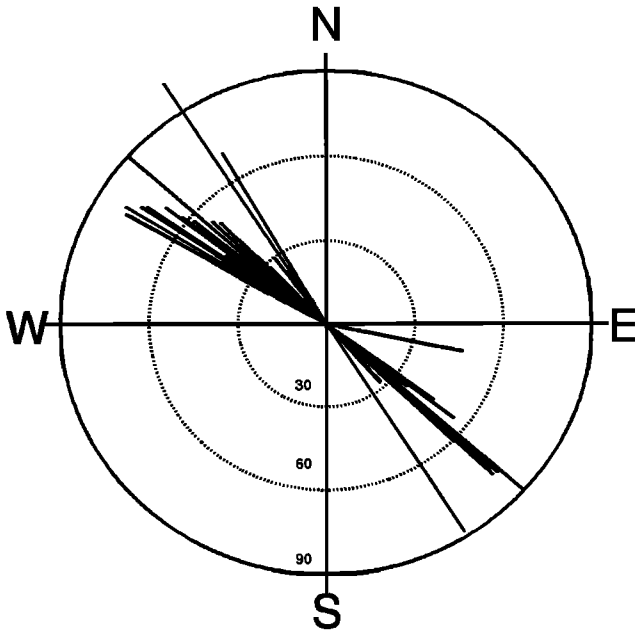


Fig. 6. Back azimuth clustering of events with initial minimal tangential components in the presence of energetic radial *P*_s components showing NW-SE orientation. Data are plotted as back azimuth (positive clockwise) versus distance in degrees (increasing outward).

southwest trending dike that may introduce a local perturbation in the receiver functions or their anisotropic properties. For these reasons, we are not overly concerned about the departure of the estimates at GRN from the rest of the array.

INFLUENCE OF SCATTERING ON ANISOTROPY ESTIMATES

As we have indicated earlier, scattering from small scale heterogeneities can induce elliptical particle motion in observed receiver functions. The effect of scattering is reduced in crustal structure determinations by stacking events from similar distances and back azimuths and restricting interpretation to coherent phases. However, since our study relies on single-station observations and specifically seeks out elliptical particle motion as a diagnostic feature of anisotropy, it is particularly vulnerable to the effects of scattering. The consistency of our results for more than 100 *P*_s phase observations and the stacking results shown in Figure 8 are arguably strong evidence that we are observing a large-scale feature of the Basin and Range crust rather than the effects of small-scale heterogeneities. Fortunately, we can supplement this argument by taking advantage of our ability to beamform data from the LAA to reduce the effects of scattering.

Randall and Owens [1992] have examined the improvement of receiver function estimates derived from beamforming over single-event, single-station estimates and stacked receiver functions at single stations in detail. The results show that by taking advantage of the array of instruments, significant improvements in the receiver function estimates can be obtained. The tangential amplitudes are decreased and the observed particle motion is less elliptical when the array is used. Since beamforming seeks to enhance aspects of the data common to all sites, it reduces the influence of small-scale heterogeneities. Thus, if scattering were a major problem in our single-event, single-station anisotropy analyses, our results would be altered significantly in beam-

formed receiver functions. To check this possibility, we examined 21 receiver functions derived by Randall and Owens [1992] using beamforming techniques with both the particle motion analysis and waveform cross-correlation procedure used on the original receiver functions where possible.

Six of the 21 receiver functions common to our study and that of Randall and Owens [1992] were among the events plotted in Figure 6 owing to their low tangential energy. After beamforming, these events still satisfied this criterion and were not analyzed further. Five other beamformed events, all from the northwest back azimuth, combined some stations with apparently interpretable *P*_s anisotropy with others satisfying the low tange-

TABLE 3. Final Results

Event	Station	Back Azimuth deg	Fast Azimuth deg	dt,s	Rank
009	GRN	285.42	100.0	0.30	B
010	GRN	233.92	50.0	0.24	B*
018	SHP	302.10	139.5	0.25	A
019	SHP	301.11	130.0	0.12	B
052	ADR	268.24	130.0	0.35	A
052	NYC	268.30	157.0	0.14	B
053	CHB	232.11	135.0	0.29	A
057	CHB	308.63	50.0	0.30	B*
059	CHB	229.50	150.0	0.13	A
068	ADR	304.97	170.0	0.14	A
068	GRN	305.02	141.0	0.33	A
068	SHP	304.93	145.0	0.25	A
068	SUN	304.93	155.0	0.22	A
076	ADR	309.90	176.0	0.24	A*
076	SHP	309.80	135.0	0.25	A
086	CHB	235.19	147.5	0.17	B
086	GRN	235.34	53.0	0.40	B
092	CHB	238.54	145.0	0.24	A*
092	GRN	238.70	80.0	0.15	B*
101	CHB	60.51	120.0	0.29	A*
104	GRN	235.22	35.0	0.35	B*
104	SUN	235.07	155.0	0.17	B*
119	GRN	234.08	75.0	0.21	B*
120	FNC	305.11	105.0	0.11	A*
122	ADR	308.40	170.0	0.22	A
122	SUN	308.33	149.0	0.27	A
125	FNC	308.24	162.0	0.24	A
130	ADR	307.66	166.0	0.21	A
137	FNC	289.11	100.0	0.12	B*
139	ADR	41.14	125.0	0.13	B*
140	SUN	41.31	115.0	0.17	B*
141	SUN	256.06	160.0	0.28	A*
151	SUN	307.35	170.0	0.24	A
151	ADR	307.41	157.0	0.26	A
153	ADR	304.69	165.0	0.23	A
168	GRN	244.14	60.0	0.15	B*
168	CHB	243.98	150.0	0.24	B*
172	CHB	234.53	150.0	0.24	B*
173	SUN	306.40	139.7	0.29	B
174	ADR	309.18	165.0	0.23	A
174	FNC	309.18	152.0	0.25	A
174	SHP	309.07	126.5	0.23	A
177	GRN	237.06	91.0	0.21	A
177	NYC	236.99	110.5	0.19	A
178	CHB	105.66	97.0	0.40	B
178	GRN	105.66	110.0	0.15	B*
179	ADR	327.38	145.0	0.31	B*
179	NYC	327.46	105.0	0.31	B*
181	SHP	235.37	50.00	0.31	B*
181	CHB	235.34	140.0	0.50	B*
182	CHB	234.21	155.0	0.20	B*
190	CHB	334.35	105.0	0.36	B
194	ADR	300.47	160.0	0.35	A
194	SHP	300.44	114.0	0.16	A
194	SUN	300.43	152.0	0.18	A

*Results based on particle motion analysis only.

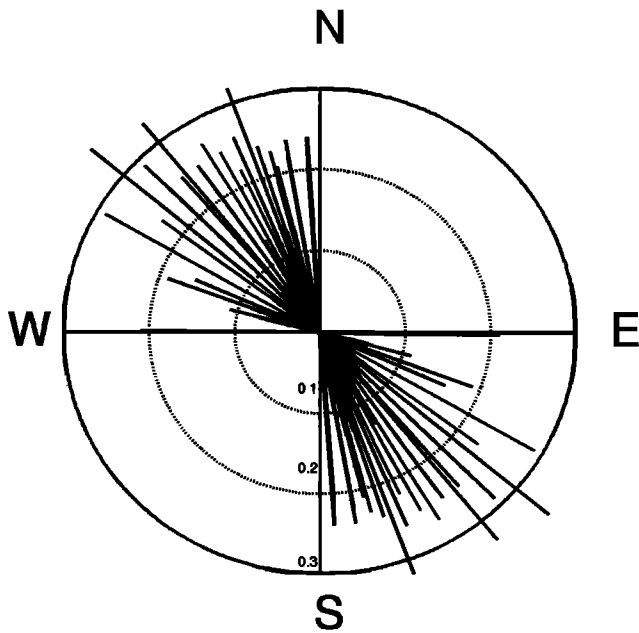


Fig. 7. "A" ranked results azimuthal diagram showing orientation (fast azimuth in degrees) and degree of anisotropy in seconds. Vectors are centered at the origin.

tial energy criteria. After beamforming, three of these events satisfied the low tangential energy criteria while the other two indicated that P_s anisotropy is present and interpretable. This demonstrates that at azimuths where minimal tangential energy is observed (and predicted from the anisotropy results), scattering is clearly influencing our analysis. Otherwise the same events for which anisotropy was identified in single-station analysis would have an anisotropic component in beamformed receiver functions.

Although this does raise concerns about the single-station observations, the fact that all such discrepancies are confined to the northwest back azimuth is not surprising given that the analyses in the previous sections indicate that the lowest tangential component excitation trends northwest-southeast. At other azimuths, the beamformed and single-station anisotropy estimates generally agree in orientation of the anisotropic axes. The agreement in time split is not as strong, with the analysis of the beamformed data indicating dt values about 0.05 s less than single-station analysis (Figure 9). This is also consistent with the conclusion that the elliptical particle motion in the P_s phase is only slightly biased by scattering effects.

Since beamforming has raised questions about the validity of our results from northwest back azimuth events, we removed them from our original fast/slow coordinate system stack and found that although slow-component P_s amplitude increased relative to the fast component (Figure 10), the split is still clearly evident. The bottom of Figure 10 shows the same procedure applied to our beamformed data set and illustrates the slight decrease in delay time in the beamformed data set. The middle traces represent synthesized P_s phases calculated using the same data distribution and a 4% velocity anisotropy throughout a 30 km-thick crust [McNamara, 1990]. These traces illustrate that the fast and slow P_s phase amplitudes should be approximately equal for the data distribution we have used. We conclude that scattering can influence our anisotropy estimates for events with small tangential amplitudes since the scattering contribution can become significant. However, the overall contribution is small

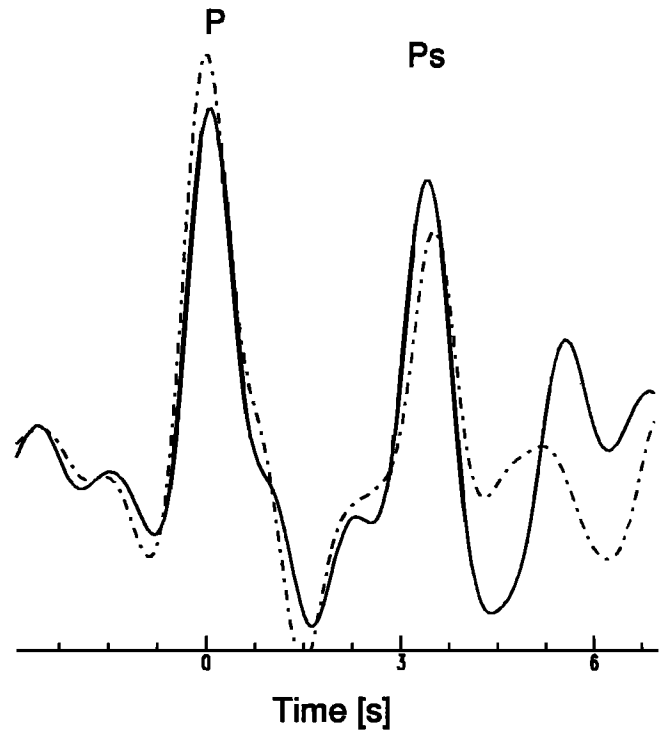


Fig. 8. 20-event stack in the fast/slow coordinate system, defined by an averaged fast azimuth estimate of 135° . Components were multiplied by either +1 or -1, depending on back azimuth, to enable stacked P_s phase components to have positive polarity for easier viewing. Solid line is the fast component; dashed line is the slow component of motion.

and primarily manifested in decreased observed split times in the analysis of beamformed data.

PETROLOGIC AND TECTONIC INTERPRETATION

After consideration of the beamformed receiver functions, we revised estimates of the ϕ and dt by eliminating B quality observations from the northwest back azimuth since they appear to be contaminated by scattering effects. This leaves us 48 observations that indicate a vector mean ϕ of 130° and dt of 0.20 derived from both single-station and beamformed events.

The most obvious association of this orientation with Basin and Range tectonics is that the estimated fast azimuth is roughly parallel to the direction of Basin and Range extension and perpendicular to the strike of most regional normal fault traces (Figure 1). The Basin and Range stress field of west central Nevada is characterized by the least principle stress oriented northwest to southeast. In a multi-data-set experiment, Zoback [1989] determined that the maximum tensile stress direction in the interior of Nevada to be oriented 120° to 135° (CNV, Figure 1). Doser

TABLE 4. Fast Azimuth and Splitting Averages for Individual Stations

Station	Fast Azimuth, deg	Split Time, s
ADR	157.2	0.24
CHB	128.7	0.28
FNC	130.0	0.18
GRN	79.5	0.25
NYC	124.2	0.21
SHP	120.0	0.22
SUN	149.5	0.23
Average	127.00	0.23

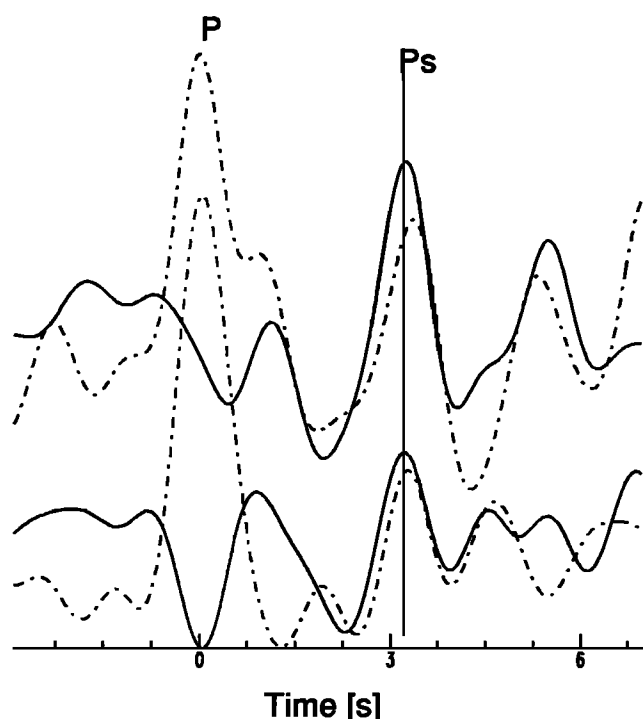


Fig. 9. (Top) Event 059 at CHB rotated to its predicted fast azimuth of 150° (see Table 3). There is a well-defined split with $\Delta t = 0.24$ s. (Bottom) Beamformed event 059 showing a reduced degree of splitting with $\Delta t = 0.19$ s. Solid line is the fast component; dashed line is the slow component in all traces shown.

[1986] analyzed all major events in the 1954-1959 Rainbow Mountain-Fairview Peak-Dixie Valley earthquake sequence using first motion and body wave modeling and obtained a minimum principle stress orientation of 126° to 128° (CNS, Figure 1). In addition, *Stock and Healy* [1988], showed that hydraulic fracture orientations and well bore elongations yield a consistent maximum principle stress orientation of 120° to 125° for the Nevada Test Site (NTS, Figure 1). As shown in Figure 1, our estimated fast azimuth range is nearly parallel to the minimum tensile stresses and thus suggests that the observed anisotropy and extensional tectonic processes are closely linked.

It is often assumed that anisotropy in the crust, particularly at shallow depths, is a result of the preferred alignment of vertically parallel microcracks [*Crampin*, 1984a, b; *Crampin et al.*, 1984a, b]. Microcracks in dilatant rock are aligned with their normals parallel to the minimum principle stress. *Crampin* [1984a] has shown that the polarization direction of fast traveling shear waves will be parallel to the plane of the crack and perpendicular to the tensile stress direction. This idea is further supported by synthetic seismogram modeling of refraction data from the 1983 Ngendei seismic refraction experiment [*Shearer and Orcutt*, 1986]. They found seismic anisotropy in the south Pacific within the top kilometer of oceanic crust and in the uppermost mantle. Crustal anisotropy was modeled as vertical cracks oriented parallel to the fast direction. This implies that the resulting fast direction is perpendicular to the fossil spreading direction in the region. Conversely, the upper mantle fast direction is parallel to fossil spreading and thus is consistent with aligned olivine crystal models of anisotropy.

The southeast trending fast azimuth calculated from our experiment data is roughly perpendicular to the dominant fracture systems in the Basin and Range and thus parallel to the direction of

maximum tensile stress. This is not consistent with models of upper crustal anisotropy, which should lead to fast azimuths parallel to fracture systems. In fact, our observed crustal anisotropy symmetry is consistent with models that are usually used to describe the preferred orientation of anisotropic minerals due to viscous flow in the mantle. *Beghoul and Baranzangi* [1990] have shown that the upper mantle lid directly beneath the Basin and Range has a maximum P_n velocity parallel to present-day extension and our observed shear wave velocity maximum. An upper mantle source can be immediately ruled out since the Ps phase is generated at the Moho, and thus any splitting must be due to an anisotropic region between the Moho and the surface. Earthquakes in this region are confined to the upper 15 km of the crust [*Vetter and Ryall*, 1983], an observation that has been explained by strain relief due to ductile flow in the lower crust [*McGarr*, 1982; *Zoback*, 1989; *Smith and Brune*, 1984]. Thus it seems reasonable to infer that the observed fast azimuth orientation is due to an anisotropic source region between about 15 and 30 km depth (the lower crust). At these depths, shearing forces due to extension can cause alignment of crystals, banding, schistosity, or foliation. Any one of these effects might be expected to give rise to anisotropy at depth [*Christensen*, 1984; *Carreras et al.*, 1980]. Furthermore, in the high heat flow environment of the Basin and Range [*Lachenbruch and Sass*, 1978], seismic velocity anisotropy could be induced by the temperature gradient and its associated

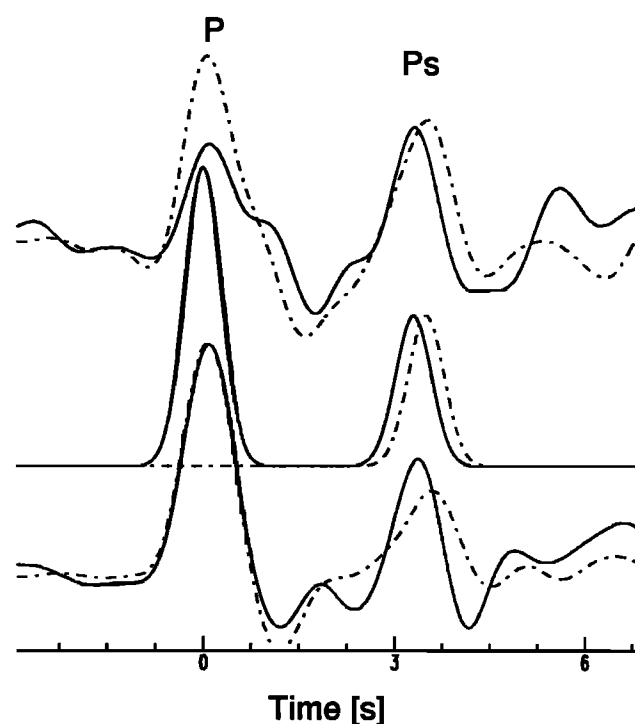


Fig. 10. (Top) 16-event stack in the fast/slow coordinate system, defined by an averaged fast azimuth estimate of 135° . Events from the northwest were removed from top stack resulting in an increased amplitude slow component relative to the fast component. (Middle) Split Ps synthetics stacked and rotated to the fast/slow coordinate system. Back azimuth distribution is similar to top stack. Synthetic shows that both components of Ps motion should be the same shape and amplitude in the fast/slow coordinate system. (Bottom) 18-event stack of beamformed receiver functions in the fast/slow coordinate system. Components were multiplied by either +1 or -1, depending back azimuth. Solid line is the fast component; dashed line is the slow component in all traces shown. Stacks were constructed in the same manner as in Fig. 8.

metamorphic gradients [Evans, 1984]. In this section, we explore possible explanations for our observations.

Layer modeling. Assuming the observed anisotropy is from a layer of lower crustal material, its thickness can be approximated by

$$L = \frac{dt \beta_o}{k}$$

where dt is the Ps phase split time, β_o is the constant shear velocity of the layer, and k is the coefficient of anisotropy or fractional difference in velocity between the fast and slow azimuths [Silver and Chan, 1988].

We used a range of geologically reasonable Ps split times and an average shear velocity of 3.6 km/s. The latter value assumed a Poisson solid and was based on our modeling and the lower crustal P velocities of Benz *et al.* [1990]. Since k is material dependent, L was computed for several candidate values (Figure 11). These values approximate the range of k that might be expected for lower crustal rocks predominantly composed of mafic and ultramafic minerals [Babuska, 1981; Christensen and Lundquist, 1982; Siegesmund *et al.*, 1989]. For the split time value dt of 0.20 s determined in this study, the anisotropic layer thickness ranges from $L = 24$ km for $k = 3\%$ to $L = 6.5$ km at $k = 11\%$ (Figure 11). Thus, for anisotropy confined to the lower 15 km of the Basin and Range crust, we must examine composition-thickness pairs with k greater than about 4.8%.

Layer composition. Since crack-induced anisotropy has been ruled out by the direction of our fast azimuth, our modeling focuses on possible preferred orientations of lower crustal minerals. For our purposes, the minerals must be length fast if they are to be consistent with the observed fast azimuth. That is, the long axis and its greatest shear velocity axis must be in the same direction in the minerals in order for the fast azimuth and Basin and Range extension to be parallel. Most felsic to mafic

minerals abundant in crustal crystalline rocks have higher anisotropy coefficients than do ultramafic minerals abundant in the upper mantle [Babuska, 1981]. Because we are possibly dealing with a large range of compositions from the midcrust to the crust-mantle transition, many mineral assemblages warrant consideration.

Minerals such as hornblende and olivine are highly length fast; however, the coefficient anisotropy k is significantly reduced in naturally occurring amphibolites and peridotites. For example, in a dunite composed of 100% olivine, k is no larger than 4% [Christensen and Lundquist, 1982]. It is possible for an olivine-rich layer to exist within the lower crust as a fractionate from upwelling gabbroic material [Furlong and Fountain, 1986]; however, it is not possible that such a layer is the exclusive source of observed shear wave splitting, since k is so small. The addition of other minerals such as pyroxene to a mafic aggregate reduces the effective whole rock anisotropy even more. In general, anisotropy in pyroxene-rich rocks such as granulites will be low relative to olivine-rich rocks, and whole rock anisotropy will decrease with increasing pyroxene content. Similar to olivine, the effective anisotropy of hornblende is diminished with the addition of other minerals to the aggregate. Laboratory measurements on clinopyroxene bearing amphibolite [Siegesmund *et al.*, 1989] show a shear velocity anisotropy of 5% that is strongly dependent on the volume fraction and orientation of hornblende. At $k = 5\%$ an amphibolite layer would need to be about 14.4 km thick. This is not consistent with current compositional models of the lower 15 km of the Basin and Range crust [Benz *et al.*, 1990; Holbrook, 1990].

Preferred orientation of minerals in metamorphic rocks. Phyllosilicates are among the most seismically anisotropic minerals. The single-crystal anisotropy coefficient is 85% for muscovite and 116% for biotite [Babuska, 1981]. The shear velocity maximum in micas is parallel to the [001] plane. The [001] plane is

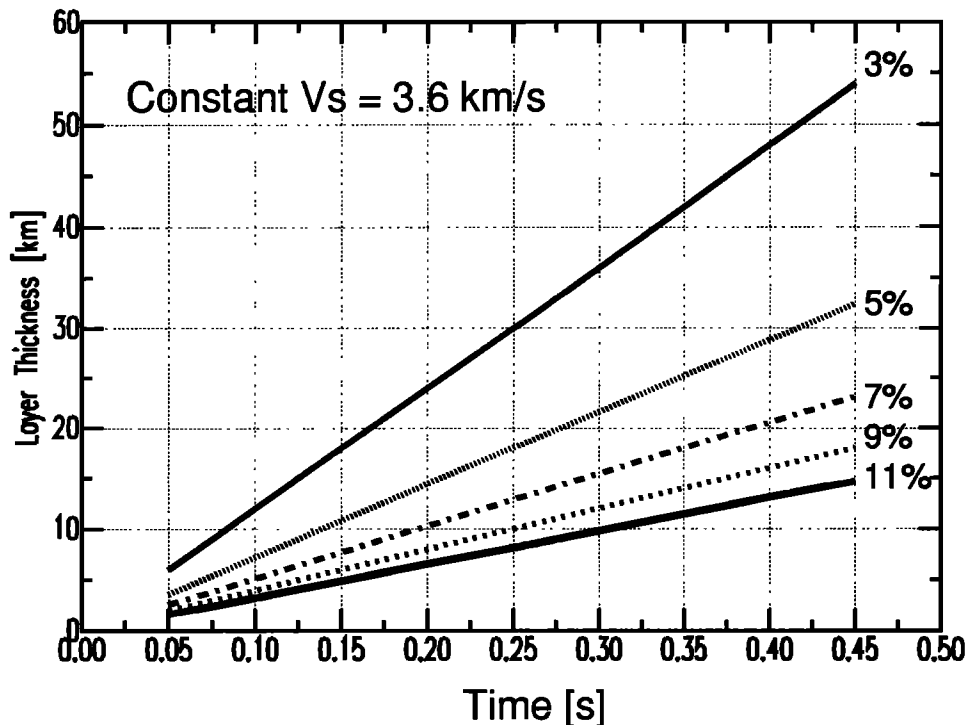


Fig. 11. Anisotropy layer thickness versus split time. Diagonal lines represent constant values of shear wave velocity difference k .

parallel to mica cleavage planes and will tend to orient normal to the maximum principle stress direction. Because of their preferred orientation and extremely high single-crystal anisotropy, micas will substantially contribute to the seismic anisotropy of rocks such as mica schists and gneisses. The preferred orientation of hornblende is also common in metamorphic rocks, and since it shares a similar anisotropic fabric with mica (i.e., length fast) both of these minerals are important factors in the orientation and resulting anisotropy of metamorphic rocks [Babuska, 1981].

In an anisotropy study involving metamorphic rocks of the Baikal rift zone, Maslova and Obolentseva [1984] analyzed four different rocks: metapelites, metamorphic granodiorites, metamorphic diorites, and metabasic rocks, in two distinct facies. The metamorphic facies considered were a low-grade greenschist and a higher-grade amphibolite-granulite. All minerals within these facies are anisotropic; however, only hornblende, micas, actinolite, and chlorite have preferred orientations and will contribute to whole rock anisotropy [Babuska, 1981]. Chlorite has anisotropy properties similar to micas, and actinolite has anisotropy properties similar to hornblende. Maslova and Obolentseva were able to calculate the group velocities for each rock, at the two different metamorphic facies, with varying degrees of mineral alignment. A *P* wave velocity difference of 51% was determined for a metapelitic rock in the greenschist facies with 90% of its constituent minerals preferentially aligned. At lower degrees of alignment, 30%, for the same rock type anisotropy was as high as 25%. Although these are *P* wave velocity differences, anisotropy of shear waves can be expected to be similar, if not greater.

Basin and Range compositional gradients modeled during the 1986 PASSCAL Nevada experiment [Benz *et al.*, 1990] suggest that at midcrustal depths, granodiorites and diorites can exist where *P* wave velocities are roughly 6.0 to 6.2 km/s. It is likely that the temperatures and stress levels in the mid to lower crust would be sufficient to induce metamorphic banding, schistosity, or foliation in the rocks present [Smith and Brune, 1984; Lachenbruch and Sass, 1978; Holbrook 1990; Holbrook *et al.*, 1991]. Using our Figure 11 and our *dt* results a layer of metamorphic granodiorite with only 30% preferential alignment of muscovite and chlorite ($k = 13\%$) would need to be 5.5 km thick. As mineral alignment increases, the degree of anisotropy also increases and the necessary layer thickness to generate shear wave splitting is reduced.

In the crustal model generated by the 1986 PASSCAL active source experiment [Benz *et al.*, 1990] felsic rocks compose roughly the upper 20 km of crust, mafics compose the remaining 10 km, and intermediate rocks, such as diorite and granodiorite, compose the transition between the upper and lower regions. Benz *et al.*, [1990] note that heat flow data suggest a temperature as high as 580°C at about 20 km depth. This suggests that intermediate composition rocks of the midcrust (granodiorite, diorite), as modeled by Benz *et al.*, [1990] should be undergoing amphibolite grade metamorphism. This region is just below the estimated depth of the brittle/ductile transition zone [Vetter and Ryall, 1983; Holbrook *et al.*, 1991; Smith and Brune, 1984], indicating that quasi-plastic flow of material would be expected to occur in response to the Basin and Range stress regime.

Holbrook [1990] and Holbrook *et al.* [1991] interpreted two-dimensional reflection data from the 1986 PASSCAL Nevada experiment and modeled a zone of strong midcrustal reflectors (10-20 km) as the brittle/ductile transition and the boundary between silicic and mafic composition. The strong reflectors were attributed to alignment of phyllosilicate minerals due to

shear stresses within this ductile, midcrustal zone. Since phyllosilicates are present in intermediate composition rocks and are known to have very strong coefficients of anisotropy, the model of Holbrook [1990] supports the idea of a midcrustal anisotropic zone beneath our array.

Several types of geological and geophysical evidence have been presented and all appear to indicate that an intermediate composition, mid to lower crustal, material undergoing metamorphism of the amphibolite grade is a distinct possibility in the Basin and Range beneath our study area. Furthermore, ductile response to Basin and Range tectonic stresses by the material appears to be both observed and expected. More information is needed on the thermal properties and composition of the Basin and Range crust, the preferential alignment of minerals in metamorphic aggregates, and the stress regime at midcrustal levels if further constraints are to be placed on this preliminary model. However, on the basis of the evidence presented it is sufficient, as a first-order model for the source of anisotropy, to conclude that a 5 to 8 km-thick midcrustal layer of preferentially aligned phyllosilicate minerals in metamorphic granodiorite or diorite fits the observed degree and orientation of Basin and Range anisotropy.

CONCLUSION

We have used Moho *P_s* phases from teleseismic receiver functions to identify and estimate shear wave anisotropy in the crust of the Basin and Range province. The previous section indicates that the orientation and amount of splitting we observe are consistent with reasonable petrologic models of the lower crust in the Basin and Range. The use of Moho *P_s* phases to study anisotropy is potentially valuable since it is one of the few ways to isolate the lower crust in the study of anisotropy. This is the first identification of shear wave anisotropy in crustal converted phases as far as we know. Thus some comments on the potential applicability of this technique are in order.

This study benefited from several aspects of both the experiment design and the Basin and Range crust in this region. First, the array of PASSCAL instruments with intermediate period sensors was designed to look primarily at teleseismic *P* waves. This allowed us two advantages over single-station receiver function methods: (1) the opportunity to make redundant observations of crustal converted phases at closely spaced stations and (2) the opportunity to use array analysis to reduce and quantify the scattering component of the *P* wave coda that can hinder single-station receiver function analysis. Next, as evidenced by our receiver functions and the 1986 PASSCAL active source experiment, the crust in this region of the Basin and Range has a prominent crust-mantle boundary. This resulted in receiver function responses with a clear Moho *P_s* phase. Therefore we are reluctant to speculate that this method will be as successful in areas with more complicated crustal structure. The use of arrays of instruments will certainly improve receiver function estimates in more complex areas, but the presence of more prominent midcrustal arrivals could obscure evidence for anisotropy. Nonetheless, this technique could represent a potentially valuable tool for separating the crustal component of shear wave anisotropy in other areas.

Acknowledgments. This work was supported by IRIS grants IRIS-0122 and IRIS-0141 to the University of Missouri and to the University of South Carolina. The foundation of the project was built by field crew

members Randy Kuehnel and Thomas Morin, who spent 10 months in the desert collecting data. The staff of the University of Nevada-Reno seismograph stations provided helpful technical support and advice as well as laboratory space for the field operations. We would also like to acknowledge the expertise and support of George Randall, Richard Boaz, and Jim Fowler, PASSCAL Project Engineer. Comments by Steve Holbrook and an anonymous reviewer helped improve our presentation and interpretation.

REFERENCES

- Allmendinger, R. W., T. A. Hauge, E. C. Hauser, C. J. Potter, S. L. Klemperer, K. D. Nelson, P. Knuepfer, and J. Oliver, Overview of the COCORP 40N transect, western United States: The fabric of an orogenic belt, *Geol. Soc. Am. Bull.*, **98**, 308-319, 1987.
- Ammon, C. J., The isolation of receiver effects from teleseismic P-waveforms, *Bull. Seismol. Soc. Am.*, **81**, 2504-2510, 1991.
- Babuska, V., Anisotropy of V_p and V_s in rock forming minerals, *J. Geophys.*, **50**, 1-6, 1981.
- Beghoul, N., and M. Baranzangi, Azimuthal anisotropy of velocity in the mantle lid beneath the Basin and Range Province, *Nature*, **348**, 536-538, 1990.
- Benz, H. M., R. B. Smith, and W. D. Mooney, Crustal structure of the Northwest Basin and Range province from the 1986 program for array seismic studies of the continental lithosphere seismic experiment, *J. Geophys. Res.*, **95**, 21,823-21,842, 1990.
- Bowman, J. R., and M. Ando, Shear-wave splitting in the upper-mantle wedge above the Tonga subduction zone, *Geophys. J. R. Astron. Soc.*, **88**, 25-41, 1987.
- Burdick, L. J., and C. A. Langston, Modeling crustal structure through the use of converted phases in teleseismic body waveforms, *Bull. Seismol. Soc. Am.*, **67**, 677-691, 1977.
- Carreras, J., P. R. Cobbold, J. G. Ramsey, and S. H. White, Shear zones in rocks, *J. Struct. Geol.*, **2**, 1-287, 1980.
- Catchings, R. D., and W. D. Mooney, Basin and Range crustal and upper mantle structure, northwest to central Nevada, *J. Geophys. Res.*, **96**, 6247-6267, 1991.
- Christensen, N. I., The magnitude symmetry and origin of upper mantle anisotropy based on fabric analysis of ultramafic tectonites, *Geophys. J. R. Astron. Soc.*, **76**, 89-111, 1984.
- Christensen, N. I., and S. M. Lundquist, Pyroxene orientation within the upper mantle, *Geol. Soc. Am. Bull.*, **93**, 279-288, 1982.
- Crampin, S., An introduction to wave propagation in anisotropic media, *Geophys. J. R. Astron. Soc.*, **76**, 17-28, 1984a.
- Crampin, S., Effective anisotropic elastic constants for wave propagation through cracked solids, *Geophys. J. R. Astron. Soc.*, **76**, 135-145, 1984b.
- Crampin, S., E. M. Chesnokov and R. G. Hipkin, Seismic anisotropy - The state of the art; II, *Geophys. J. R. Astron. Soc.*, **76**, 1-16, 1984a.
- Crampin, S., R. Evans, and B. K. Atkinson, Earthquake prediction: A new physical basis, *Geophys. J. R. Astron. Soc.*, **76**, 147-156, 1984b.
- DeMets, C., R. G. Gordon, S. Stein, and D. F. Argus, A revised estimate of Pacific-North American motion for western North America plate boundary zone tectonics, *Geophys. Res. Lett.*, **14**, 911-914, 1987.
- Doser, D. I., Earthquake processes in the Rainbow Mountain-Fairview Peak-Dixie valley, Nevada, region 1954-1959, *J. Geophys. Res.*, **91**, 12,572-12,586, 1986.
- Eaton, J. P., Crustal structure from San Francisco, California, to Eureka, Nevada, from seismic refraction measurements, *J. Geophys. Res.*, **68**, 5789-5806, 1963.
- Evans, R., Anisotropy: A pervasive feature of fault zones, *Geophys. J. R. Astron. Soc.*, **76**, 157-163, 1984.
- Farmer, G. L., and D. J. DePaolo, Origin of Mesozoic and Tertiary granite in the western United States and implications for pre-Mesozoic crustal structure 1. Nd and Sr isotopic studies in the geocline of the northern Basin and Range, *J. Geophys. Res.*, **88**, 3379-3401, 1983.
- Furlong, P. F., and D. M. Fountain, Continental crustal underplating: Thermal considerations and seismic-petrologic consequences, *J. Geophys. Res.*, **91**, 8285-8294, 1986.
- Hague, T. A., R. W. Allmendinger, C. Caruso, E. C. Hauser, S. L. Klemperer, S. Opdyke, C. J. Potter, W. Sanford, L. Brown, S. Kaufman, and J. Oliver, Crustal structure of western Nevada from COCORP deep seismic-reflection data, *Geol. Soc. Am. Bull.*, **98**, 320-329, 1987.
- Holbrook, W. S., The crustal structure of the northwestern Basin and Range province, Nevada, from wide-angle seismic data, *J. Geophys. Res.*, **95**, 21,843-21,869, 1990.
- Holbrook, W. S., R. D. Catchings, and C. M. Jarchow, Origin of deep crustal reflections: Implications of coincident seismic refraction and reflection data in Nevada, *Geology*, **19**, 175-179, 1991.
- Klemperer, L. L., T. A. Hauge, E. C. Hauser, J. E. Oliver, and C. J. Potter, The Moho in the northern Basin and Range province, Nevada, along the COCORP 40N seismic reflection transect, *Geol. Soc. Am. Bull.*, **97**, 603, 1986.
- Kosarev, G. L., L. I. Makeyeva, and L. P. Vinnik, Anisotropy of the mantle inferred from observations of P to S converted waves, *Geophys. J. R. Astron. Soc.*, **76**, 209-220, 1984.
- Lachenbruch, A. H., and J. H. Sass, Models of an extending lithosphere and heat flow on the Basin and Range province, in *Cenozoic Tectonics and Regional Geophysics of the Western Cordillera*, edited by R. B. Smith and G. P. Eaton, *Mem. Geol. Soc. of Am.*, **152**, pp. 209-250, 1978.
- Langston, C. A., The effect of planar dipping structure on source and receiver responses for constant ray parameter, *Bull. Seismol. Soc. Am.*, **67**, 1029-1050, 1977.
- Langston, C. A., Structure under Mount Rainier, Washington, inferred from teleseismic body waves, *J. Geophys. Res.*, **84**, 4749-4762, 1979.
- Langston, C. A., Scattering of teleseismic body waves under Pasadena, California, *J. Geophys. Res.*, **94**, 1935-1951, 1989.
- Maslova, S. I., and I. R. Obolentseva, An anisotropic model of the Earth's crust in the Baikal rift zone, *Geophys. J. R. Astron. Soc.*, **76**, 227-232, 1984.
- McGarr, A., Analysis of states of stress between provinces of constant stress, *J. Geophys. Res.*, **87**, 9279-9288, 1982.
- McNamara, D. E., Evidence for azimuthal seismic velocity anisotropy in the Basin and Range province: Implications for middle to lower crustal tectonic processes, M.S. thesis, Univ. of Missouri, Columbia, 1990.
- Minster, J. B., and T. H. Jordan, Vector constraints on western U.S. deformations from space geodesy, neotectonics, and plate motions, *J. Geophys. Res.*, **92**, 4798-4804, 1987.
- Nakanishi, K. K., J. J. Zucca, B. C. Bowman, D. W. Ewert, P. E. Harben, S. P. Jarpe, C. A. Johnston, and D. W. Rock, The LLNL Configurable Seismic Monitoring System, Final Report, *Lawrence Livermore Lab. Rep. UCRL-ID-108241*, 1991.
- Owens, T. J., Crustal structure of the Adirondack mountains determined from broadband teleseismic waveform modeling, *J. Geophys. Res.*, **92**, 6391-6401, 1987.
- Owens, T. J., and R. S. Crosson, Shallow structure effects on broadband teleseismic P waveforms, *Bull. Seismol. Soc. Am.*, **78**, 96-108, 1988.
- Owens, T. J., G. Zandt, and S. R. Taylor, Seismic evidence for an ancient rift beneath the Cumberland Plateau, Tennessee: A detailed analysis of broadband teleseismic P waveforms, *J. Geophys. Res.*, **89**, 7783-7795, 1984.
- Owens, T. J., and G. E. Randall, Data report for the 1988-89 PASSCAL Basin and Range Passive-source Seismic Experiment Part 1: large aperture array data, *PASSCAL Data Rep. 90-001*, IRIS, Wash. D.C., 1990.
- Owens, T. J., D. E. McNamara, G. Zandt, K. F. Priestley, and G. E. Randall, Array analysis of teleseismic receiver functions using PASSCAL Basin and Range Passive-source Experiment data (abstract), *Seismol. Res. Lett.*, **60**, 20, 1989.
- Pakiser, L. C., Structure of the crust and upper mantle in the western United States, *J. Geophys. Res.*, **68**, 5747-5756, 1963.
- Phinney, R. A., Structure of the Earth's crust from spectral behavior of long-period body waves, *J. Geophys. Res.*, **69**, 2997-3017, 1964.
- Priestley, K. F., A. S. Ryall, and G. S. Fezie, Crust and upper mantle structure in the northwest Basin and Range province, *Bull. Seismol. Soc. Am.*, **72**, 911, 1982.
- Prodehl, C., Seismic refraction study of crustal structure in the western United States, *Geol. Soc. Am. Bull.*, **81**, 2629-2646, 1970.
- Prodehl, C., Crustal structure of the western United States, *U.S. Geol. Surv. Prof. Pap.* **1034**, 74 pp., 1979.
- Randall, G. E., and T. J. Owens, Array Analysis of teleseismic P-waveforms from the 1988-89 PASSCAL Basin and Range Passive Source Seismic Experiment, in press, *Geophys. J. Int.*, 1993.
- Savage, M. K., X. R. Shih, R. P. Meyer, and R. C. Aster, Shear-wave anisotropy of active regions via automated S-wave polarization analysis, *Tectonophysics*, **165**, 279-292, 1989.
- Savage, M. K., W. A. Peppin, and U. R. Vetter, Shear-wave anisotropy and stress direction in and near Long Valley Caldera, California, *J. Geophys. Res.*, **95**, 11,165-11,177, 1990a.
- Savage, M. K., P. G. Silver, and R. P. Meyer, Observations of teleseismic

- shear-wave splitting in the Basin and Range from portable and permanent stations, *Geophys. Res. Lett.*, *17*, 21-24, 1990b.
- Shearer, P. M., and J. A. Orcutt, Compressional and shear wave anisotropy in the oceanic lithosphere-The Ngendei seismic refraction experiment, *Geophys. J. R. Astron. Soc.*, *87*, 967-1003, 1986.
- Shih, X. R., R. P. Meyer, and J. F. Schneider, An automated analytical method to determine shear-wave splitting, *Tectonophysics*, *165*, 271-278, 1989.
- Siegesmund, S., T. Takeshita, and H. Kern, Anisotropy of V_p and V_s in an amphibolite of the deeper crust and its relationship to the mineralogical, microstructural and textural characteristics of the rock, *Tectonophysics*, *157*, 25-38, 1989.
- Silver, P. G., and W. W. Chan, Implications for continental structure and evolution from seismic anisotropy, *Nature*, *335*, 34-39, 1988.
- Silver, P. G., and W. W. Chan, Shear wave splitting and subcontinental mantle deformation, *J. Geophys. Res.*, *96*, 16,429-16,454, 1991.
- Smith, R. B., and R. L. Brune, Intraplate extensional tectonics of the eastern Basin-Range: Inferences on structural style from seismic reflection data, regional tectonics, and thermal-mechanical models of brittle-ductile deformation, *J. Geophys. Res.*, *89*, 5733-5762, 1984.
- Speed, R. C., Alison M. W., and F. R. Heck, Phanerozoic tectonic history of North America in the Great Basin, in *Metamorphism and Crustal Evolution of the Western United States*, edited by W. G. Ernst, pp. 572-606, Prentice Hall, Englewood Cliffs, N. J., 1987.
- Stauber, D. A., Crustal structure in northern Nevada from seismic reflection data, 319 pp., *Geotherm. Resour. Council Spec. Rep.*, *13*, 1983.
- Stauber, D. A., and D. M. Boore, Crustal thickness in northern Nevada from refraction profiles, *Bull. Seismol. Soc. Am.*, *68*, 1049-1058, 1978.
- Stock, J. M., and J. H. Healy, Stress field at Yucca Mountain, Nevada, *U. S. Geol. Surv. Bull.*, *1170*, 87-93, 1988.
- Taylor, S. R., and H. J. Patton, Shear-velocity structure from regionalized surface-wave dispersion in the Basin and Range, *Geophys. Res. Lett.*, *13*, 30-33, 1986.
- Thompson, G. A., and D. B. Burke, Regional geophysics of the Basin and Range province, *Annu. Rev. Earth Planet. Sci.*, *2*, 213-238, 1974.
- Vetter, U. R., and A. S. Ryall, Systematic change of focal mechanism with depth in the Western Great Basin, *J. Geophys. Res.*, *88*, 8237-8250, 1983.
- Zoback, M. L., State of stress and modern deformation of the northern Basin and Range province of the western United States, *J. Geophys. Res.*, *94*, 7105-7128, 1989.

D. E. McNamara and T. J. Owens, Department of Geological Sciences, University of South Carolina, Columbia, SC 29208.

(Received December 30, 1991;
revised March 5, 1993;
accepted March 8, 1993)